Research Article | Vol. 31, No. 25 / 4 Dec 2023 / Optics Express 41569
Optics EXPRESS

Surface plasmon resonance sensor based on polarization parameter SPR imaging

ZHENG CHE,[1] JAMIE JIANGMIN HOU,[2] LIANPING HOU,[3] BIN NI,[1] XUEFENG LIU,[1] BIN XU,[1,4,†] AND JICHUAN XIONG[1,5,†]

[1]School of Electronic and Optical Engineering, Nanjing University of Science and Technology, Nanjing 210094, China
[2]Department of Medicine, University of Cambridge, Hills Road, Cambridge CB2 0QQ, UK
[3]James Watt School of Engineering, University of Glasgow, Glasgow G12 8QQ, UK
[4]xubinhit13@163.com
[5]Jichuan.xiong@njust.edu.cn
[†]Co-last authors

Abstract: Using polarization surface plasmon resonance (SPR) imaging as a sensor has the advantage of large throughput in detection, but its sensitivity has always been inferior to other SPR sensors. The high contrast of the two polarization parameters' images related to scattering determines the high sensitivity of this new polarization SPR imaging sensor. It provides a new direction for solving the issue of low sensitivity in polarization SPR imaging. The sensor system was optimized by numerical simulation, whilst the baseline noise and sensitivity of the system were obtained by saline solution and virus detection. When the reflective index of the NaCl solution is within the range of 1.3331 to 1.36, the average sensitivity can reach 9300 RIU^{-1}, and the maximum sensitivity can reach 13000 RIU^{-1}. Using this new polarization SPR imaging sensor, the H1N1 virus was differentiated, showing its promising application potential within the field of biomedicine.

1. Introduction

As an optical sensor, surface plasmon resonance (SPR) imaging mainly relies on the change in the incident light intensity absorption at different angles due to the change in the ambient refractive index (RI) at the interface between the dielectric and the metal sheet to obtain high-contrast imaging [1–3]. Theoretically, the phase-matching conditions that excite SPR result in a single wavelength of light. Experimentally, it will result in a narrower bandwidth due to dispersion within the material. Changing any one of the excitation condition parameters whilst keeping other parameters fixed, such as changing the surface RI, will cause a measurable wavelength band shift in the SPR spectrum, from which the RI of the dielectric medium can be calculated. Due to its precise detection performance, research interest in SPR imaging has rapidly expanded, along with widespread applications within the food safety [4,5], medical detection [5–13], environmental monitoring [14,15], and chemical manufacture [16–19] industries.

Depending on the excitation conditions, SPR imaging can be divided into intensity SPR imaging [20], spectral SPR imaging [21] and phase or polarization contrast SPR imaging [22–26]. Intensity SPR imaging sensors are the most widely used method. Among the different detection methods, phase SPR imaging is by far the most sensitive technique, however, its practical use is limited by its inherent sensitivity to background noise. Compared with traditional SPR sensors, though SPR imaging sensors have the advantage of large-throughput detection, their detection sensitivity is about an order of magnitude lower than other traditional SPR sensors, which limits their potentially wide applications. Polarization contrast SPR imaging based on conventional SPR imaging was first proposed by Piliarik and Homola in 2005 [22]. Polarization contrast SPR imaging has a single incident angle and incident wavelength. It converts the phase change caused

#506158 https://doi.org/10.1364/OE.506158
Journal © 2023 Received 18 Sep 2023; revised 29 Oct 2023; accepted 12 Nov 2023; published 27 Nov 2023

Optics EXPRESS

by the SPR into the change in light intensity to realize the detection of the sample by using a charge-coupled device (CCD) as a detector. As polarization contrast SPR imaging essentially uses the light intensity signal detected by a CCD to represent the change of phase information, this scheme not only has higher sensitivity and wider dynamic detection range than other SPR imaging types but also has a simple optical system and is easy to implement. These advantages make polarization contrast SPR imaging very promising. Later, Piliarik improved the sensor resolution by one order of magnitude with the subtraction of the dark current signal and intensity fluctuations of the light source [27]. Patskovsky proposed a scheme of spatially modulated surface plasmon resonance polarimetry [28]. A birefringent wedge was utilized to produce periodic changes in phase relations between the p-polarized and s-polarized light, and they were allowed to interfere after passing through an analyzer at an orientation of 45°. The Fourier transform method was used for phase extraction. Han presented an ellipsometric SPR imaging system [29] in which the prism-based SPR sensor head was located between a polarizer and an analyzer. The analyzer was rotated at three different angles, and the subsequent intensity images were used to calculate the phase and ellipsometric parameters. Y. Mikhyeyev used polarization SPR imaging to catch the water and silicon oil mixture picture on the surface of silver-coated crossed surface relief gratings [30]. It records the 1D or 2D spatial distribution of SPR signal intensity using a high dynamic range camera and analyzes it as a function of RI changes.

In this paper, we present a new SPR imaging sensor called polarization parameter SPR imaging. This sensor can acquire two kinds of result ($\sin\delta$ and φ). Firstly, we acquired two main parameters in theoretical calculations and proved their sensitive response in the system. Secondly, we optimized polarization parameter SPR imaging system parameters through the finite-difference time-domain (FDTD) method and used them to build the polarization parameter SPR imaging sensor system. For all FDTD simulations in this work, the perfectly-matched-layer (PML) boundary conditions were used on all boundaries. Thirdly, the baseline noise, sensitivity and recognition results of the system were obtained using saline solution and H1N1 virus in the experiment setup. Compared with other polarized SPR imaging methods according to table. 1, the advantages of our sensor are obvious. First, high sensitivity can be achieved using only a simple sensor material chip structure. Second, with the introduction of two parameters, a wide dynamic range of refractive index can be maintained at the same time of higher sensitivity. Third, this new sensor detection method, encompassing possibilities like polarizer control and sensor chip design. Fourth, as a new sensing mode, it has broad prospects for development.

Table 1. Compared with the sensitivity of the intensity sensor in recent years.

Year	SPR Imaging mode	Model	Refractive index range (RIU)	Sensitivity (RIU-1)	Ref.
2021	Intensity	Prism/Cytop/ITO/TMDC	1.32-1.34	6695	[31]
2021	Intensity	Prism/MgF2/Al/Antimonene	1.33-1.38	7028	[32]
2021	Intensity	Prism/Gold	1.3330-1.33367	7589.18	[33]
2023	Intensity	Prism/LiF/Ag/Si/WS2	1.38	7884.71	[34]
2023	Intensity	Prism/Bp/MoS2/Graphene	1.33-1.355	9778.9 (Maximum)	[35]
2019	Polarization contrast	Prism/Graphene/Gold	-	12300	[26]
Our work	Polarization parameter	Prism/Cr/Gold	1.335-1.365	13000 (Maximum) 9402 (Average)	-

Optics EXPRESS

2. Theory

The classical polarization SPR imaging system has a fixed incident light angle and wavelength, then uses linear polarization to excite SPR. After the SPR excitation, the reflected light changes to elliptically polarized light. A quarter-wave plate and a linear polarizer is added to the reflected light optical path, and the fast axis of the quarter-wave plate is adjusted to coincide with the elliptically polarized light. The elliptically polarized light is changed into linearly polarized light after passing through the quarter-wave plate, then the follow-up linear polarizers are adjusted to be in the orthogonal state to complete the extinction. When the RI of the medium changes, the phase shift of the p-polarized light component changes, the polarization state of the reflected light changes, and the intensity of the transmitted light through the wave plate and polarizer increases [36].

The excitation of SPP is the key to polarization SPR imaging sensing. The SPR is excited by the evanescent wave that is generated by the incident light at the interface. When the incident light plane is x-z, the wave vector perpendicular to the two interfaces can be expressed as:

$$k_z{}^2 = n_1{}^2(\frac{2\pi}{\lambda})^2(\frac{n_1{}^2}{n_2{}^2} - \sin\theta_1) \tag{1}$$

where n_1, n_2 are the RI of the medium on each side of the interface, and θ_1 is the incident angle.

Due to the structural gap limitations of the Otto structure, SPR imaging sensors are mostly based on the Kretschmann's structure [37]. Kretschmann's three-layer film reflection model is shown in Fig. 1. When the incident light is reflected by the metal layer, reflected light intensity for the s-polarized light and p-polarized light ($R_{s/p}$) is:

$$R_{s/p} = |r_{s/p}|^2 = \left|\frac{r_{1-2} + r_{2-3}\exp(i\delta)}{1 + r_{1-2}r_{2-3}\exp(i\delta)}\right|^2 \tag{2}$$

The reflection coefficient at the interface between the prism and the metal layer is denoted as r_{1-2}, while r_{2-3} represents the reflection coefficient at the metal-air interface. Additionally, we define $\delta = 2k_z d$, where d signifies the thickness of the metal layer.

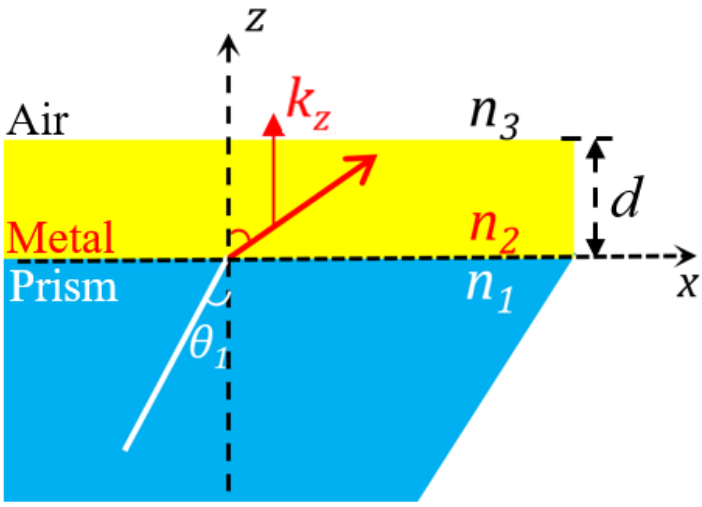

Fig. 1. Kretschmann's three-layer film model.

Optics EXPRESS

If the incident light is linearly polarized at the polarization angle θ_0, the intensity of the reflected light I_0 can be expressed:

$$I_0 = |r_s \cos\theta_0|^2 + |r_p \sin\theta_0|^2 \tag{3}$$

When the incident light is a p-polarized light, the polarizer angle θ_0 is 90°, the polarizer and prism constitute the basic structure of the intensity SPR imaging.

When the collimated light passes through the rotating polarizer to become linearly polarized light, total reflection occurs at the prism-metal film interface, the surface of the metal film excites SPR, and then the reflected light is received by the camera through the quarter-wave plate and the analyzer. For each polarization angle θ_i, there is an I_i corresponding to it:

$$I_i = \frac{{r_s}^2 + {r_p}^2}{2} + \frac{{r_s}^2 - {r_p}^2}{2}\cos 2\theta_i + r_s r_p \sin(\varphi_s - \varphi_p)\sin 2\theta_i \tag{4}$$

Let $k_0 = \frac{{r_s}^2+{r_p}^2}{2}$, $k_1 = \frac{{r_s}^2-{r_p}^2}{2}$, $k_2 = r_s r_p \sin(\varphi_s - \varphi_p)$ the data points in the experiment show that the light intensity signal is collected equidistantly within a cycle, the Fourier series can be fitted and a periodic function can be derived. When the incident wavelength and the incident angle are fixed (but not to the polarization angle of the incident light), the r_p, r_s, φ_p *and* φ_s are only related to the refractive index of the dielectric layer. The k_0, k_1, k_2 are essentially the coefficients of trigonometric functions of different frequencies, so the periodic discrete data points in the experiment can be fitted using Fourier series, and then we can get:

$$\sin\delta = \sin(\varphi_s - \varphi_p) = \frac{k_2}{\sqrt{{k_0}^2 - {k_1}^2}} \tag{5}$$

After total reflection by the prism, the orientation of the reflected light vector changes to:

$$\tan\theta_2 = \frac{r_s}{r_p}\tan\theta_1 \tag{6}$$

For the convenience of expression, the direction angle change coefficient is defined as:

$$\varphi = \frac{r_s}{r_p} \tag{7}$$

The polarization parameter SPR imaging performs an inversion calculation on the pixels at the same position in all of the original image data that were collected in one cycle. From this we can obtain the phase difference sinδ parameter value and the direction angle change coefficient φ parameter calculated by this pixel during the modulation process, return the normalized parameter value to the original position, and operate on other pixels in sequence. Finally, two images are generated which reflects the normalized phase difference sinδ, whilst the direction angle change coefficient φ reflect the change of SPR excitation to the polarization of the incident line parameter image.

3. Experiment setup

After theoretical analysis, we found that the two parameters are very sensitive to the change in the medium RI between 1.32 to 1.35, so we built a model of the excitation optical system. The schematic diagram of the complete polarization parameter SPR imaging system is shown in Fig. 2. HL is a halogen lamp source, LCTBF is a liquid crystal tunable filter. L1, L2 and L3 are convex lenses. D1 is diaphragm. D2 is aperture. BE is a beam expander. D3 is a rectangular aperture. P1 is polarizer. QWP is quarter wave plate. P2 is analyzer. C is camera. The incident light is emitted by a halogen lamp (HL) through the collimation system and a polarizer convert it

Optics EXPRESS

into a linearly polarized light to excite SPR. The reflected light is captured by a CCD and is used for imaging and data analyzing. In the SPR excitation part of the system, we adopted the strategy of coupling Microflow-Cell chip with a metal layer, adhesive, and prism to achieve the purpose of sensing biological samples.

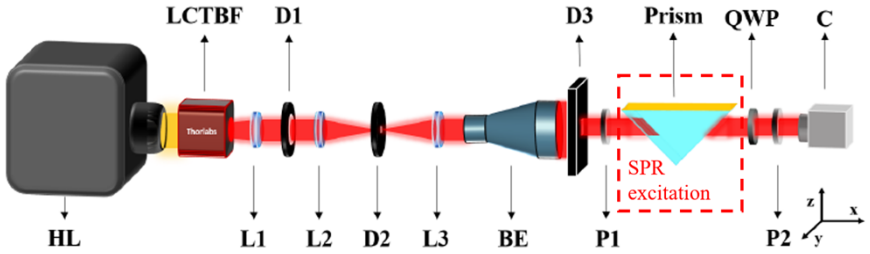

Fig. 2. Schematic of the polarization SPR imaging system model.

Compared with other metals, gold is chemically stable and has good reproducibility, so we choose gold as the material for the metal layer of the prism and Cr as the adhesive layer between gold layer and prism. In most SPR studies, the sensing system is most sensitive when the thickness of the gold film in the Kretschmann structure is 50 nm [37].

3.1. Determination of system parameters

As the Cr layer can provide the conditions for multiplexing sensor chips, we first consider how the thickness of this adhesion promoter influences the SPR excitation. In our FDTD simulation, we use a p-polarized light source with a wavelength of 633 nm, the thickness of the gold film layer is 50 nm, and the prism is K9 glass (n_1=1.517 at 590 nm wavelength). The Y and Z-direction boundary conditions were set as Bloch Periodic boundary condition, while the X-direction boundary condition was defined as a Perfectly Matched Layer (PML) boundary condition. The mesh size was specified as 2 nm × 2 nm × 2 nm. The influence of the Cr layer thickness (0-5 nm) on the resonance peak of the system is shown in Fig. 3(a). Curve fitting the resonance angle as a function of the thickness of Cr is shown in the inset of Fig. 3(a), where the resonance angle will shift about 0.074° for every 1 nm thicker Cr layer (Fig. 3(c)). The resolution of the SPR sensor can be compared by looking at the FWHM of the SPR reflectivity dip curve. The larger the FWHM, the greater the resolution and the lower the detection accuracy [38]. According to Fig. 3(b), it can be seen that as the Cr layer thickness increases, the sensitivity of the sensing system decreases, and the resolution of the sensing system increases.

Second, we use FDTD to simulate two mainstream prisms (JGS1 glass and K9 glass) used in SPR imaging. At 633 nm, the refractive index of JGS1 glass and K9 glass are 1.457 and 1.515. We set the thickness of the Cr layer to 2 nm and the thickness of the Au layer to 50 nm, the incident light is 633 nm, the p-polarized light is incident during the medium RI scanning, and the medium RI is pure water 1.33 during the angle scanning. X-direction boundary condition was defined as a PML boundary. And Y-direction and Z-direction boundary conditions were set as Bloch periodic boundaries. The mesh size was setting as 2 nm × 2 nm × 2 nm. The reflectivity as a function of the incident angle and RI of the medium is shown in Fig. 4(a) and Fig. 4(b) respectively. In the medium scanning curve, a curve with a width of 0.1 RI is intercepted for linear fitting, the slopes of the JGS1 prism and K9 prism curves are 32.4 and 29.5, which means the sensitivity of JGS1 is better than that of K9. The detection range of K9 prism is larger than that of JGS1 prism. The resonance angles of the JGS1 prism and K9 prism are 80.1° and 72° respectively. The RI of the prism has a great influence on the resonance angle. The smaller the RI of the prism, the larger the resonance angle. At the same time, as the RI of the prism

Optics EXPRESS

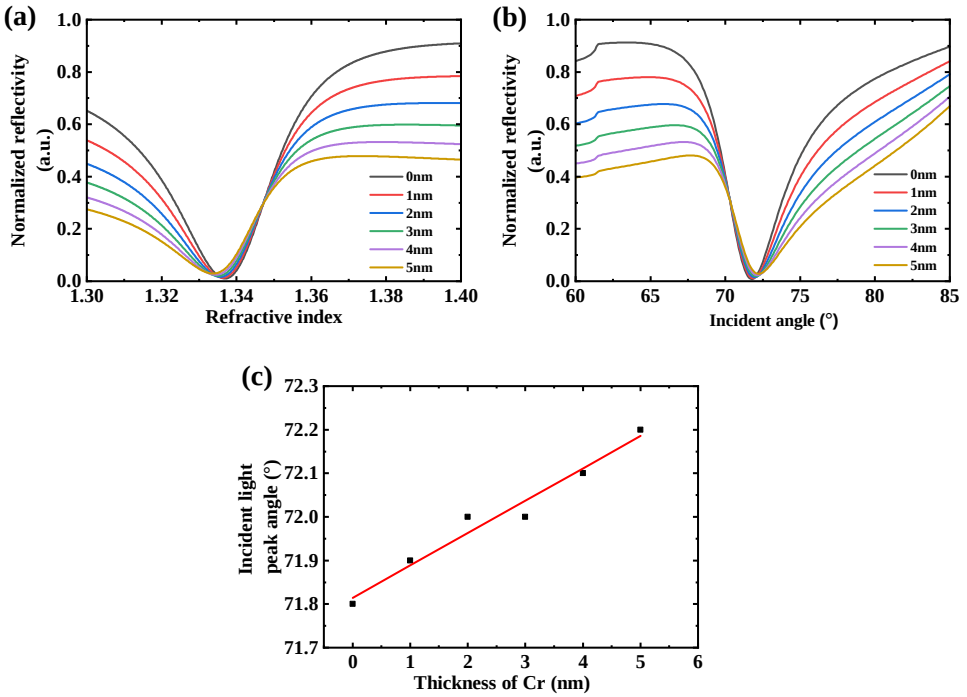

Fig. 3. Effect of different thicknesses of Cr layer. (a) Influence curve of Cr layer thickness (the thickness change from 0 nm to 5 nm in 1 nm) in medium RI from 1.3 to 1.4 on reflectivity. (b) Influence curve of Cr layer thickness (the thickness change from 0 nm to 5 nm in 1 nm) on the RI under the incident light (incident angle from 60° to 85°). (c) Resonance angle fitting curve different thickness Cr layer (the thickness change from 0 nm to 5 nm in 1 nm).

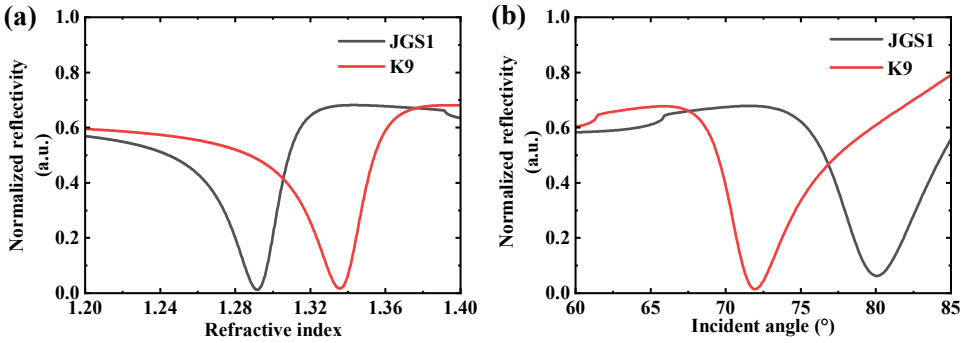

Fig. 4. Effect of different prisms. (a) Influence curve of JGS1 and K9 on reflectivity under medium RI from 1.2 to 1.4. (b) Influence curve of JGS1 and K9 on the RI under the incident light (incident angle from 60° to 85°).

decreases, the resolution increases, the detection accuracy of the system decreases. Finally, K9 glass was chosen as the designated prism.

In terms of choosing a wavelength for the system light source, FDTD was used to simulate different light source wavelength effects on SPR excitation in 1.33 background RI. PML boundary set in X-direction, and Bloch periodic boundaries set in Y-direction and Z-direction. The mesh size was setting as 2 nm × 2 nm × 2 nm. The prism is set to be K9 glass, the thickness of the Cr layer is 2 nm, the thickness of the Au layer is 50 nm, and the incident angle is scanning from 60° to 85°. According to the results in Fig. 5, increase in wavelength has a positive effect on the

Optics EXPRESS

sensing performance in terms of the resolution. Taking into account the practical applications and operational difficulty, the incident wavelength should be below 650 nm. In addition, in order to reduce the complexity of the system, the collimated light is along the horizontal direction.

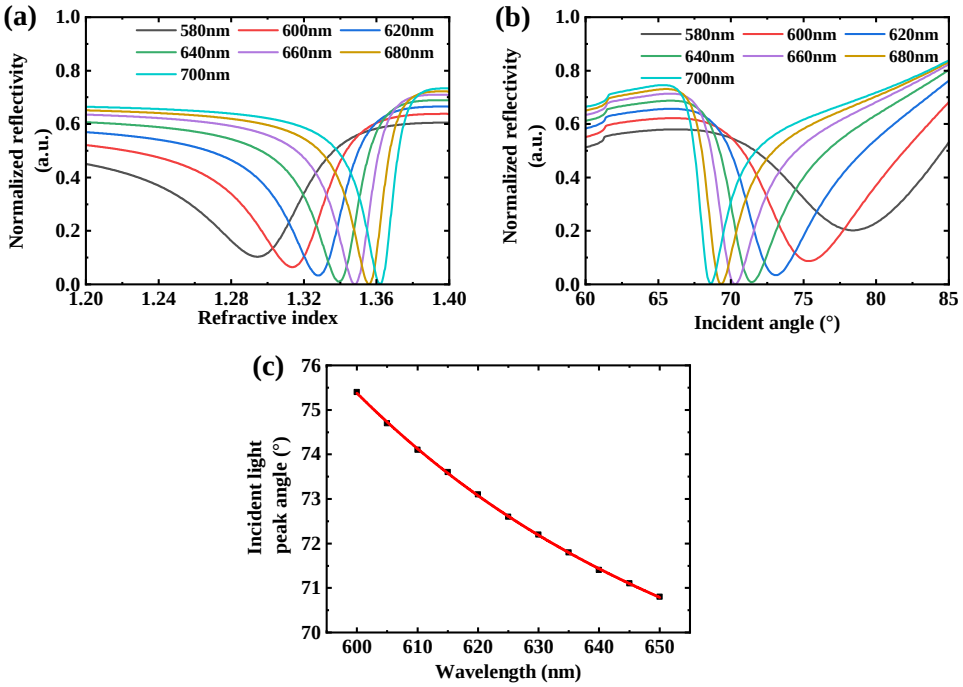

Fig. 5. Effect of different wavelength. (a) Influence curve of different wavelength (from 580 nm to 700 nm in 20 nm) light source in medium RI from 1.2 to 1.4 on reflectivity. (b) Influence curve of different wavelength (from 580 nm to 700 nm in 20 nm) light source on the RI under the incident light (incident angle from 60° to 85°). (c) Resonance angle fitting curve of different wavelength light source (from 580 nm to 700 nm in 20 nm).

3.2. Microflow-Cell chip

The range of RI for the detection of biomolecules is generally around 1.33 to 1.36. Traditional biological sample loading equipment will receive serious stray light interference in the system. To overcome this problem, the specific layout and dimensions of the Microflow-Cell chip are shown in Fig. 6(a).

There are 2 rows and 5 columns of microflow detection channels. The horizontal spacing between grooves was set to 3.0 mm and the vertical spacing was set to 2 mm. The sensor chip is processed using a glass-refined carved machine. Each sensor chip is composed of two K9 glass pieces. One of which is a 0.5 mm thick upper piece. The sculpture machine is used to dig 10 penetration pores on the upper cover according to the chip design scheme. Then use ultraviolet curing glue (UV glue) with a RI of 1.62 to glue the upper cover sheet to the lower layer sheet with a thickness of 1 mm and the same size. The penetration holes and the lower layer sheet constitute 10 detection channels. After the sensor chip is glued, ultrasonic cleaning is carried out. Then, the magnetron sputtering coating equipment is used to coat the surface of the microflow pool chip with an Au layer. The physical fabricated Microflow-Cell chip is shown in Fig. 6(b).

Optics EXPRESS

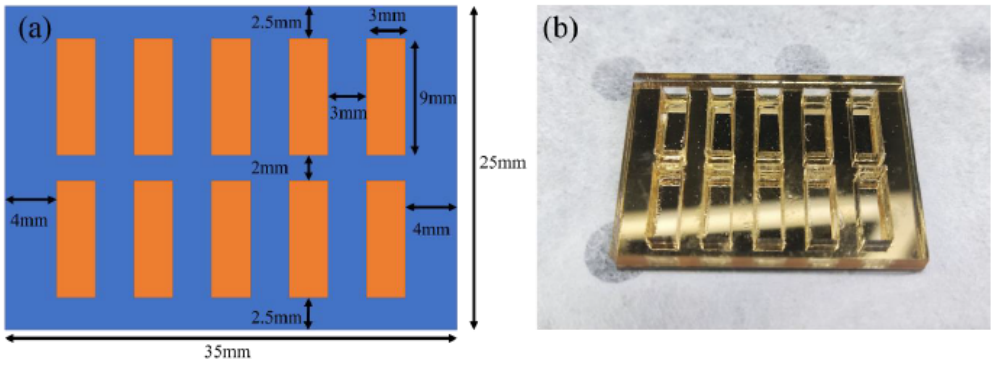

Fig. 6. Microflow-Cell chip structure of (a) designed layout, and (b) fabricated chips.

3.3. System setup

According to the above optimization, the polarization parameter SPR imaging sensing experiment system is as shown in Fig. 7. A halogen light source was used to provide a wide-band beam of 550 nm to 675 nm. The beam was incident to the SPR excitation section through a collimation system combined with Kohler illumination and a rectangular aperture (to control the beam size). The prism in the excitation section is made of K9 glass, prism dimensions are 25.4 mm × 25.4 mm × 25.4 mm. The Cr layer, serving as an adhesion promoter, has a thickness of 2 nm. The metal layer (Au) is 50 nm. The quarter-wave plate is at a 45° to the incident plane, and the analyzer is parallel to the incident plane. In SPR excitation part we use a special fixture to hold the prism.

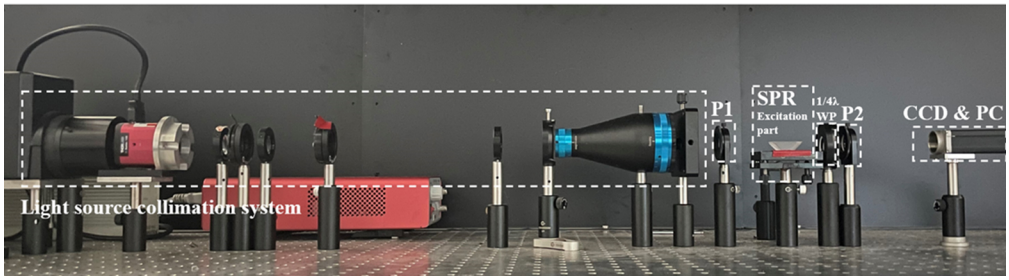

Fig. 7. Experiment setup. Each part is built as shown in Fig. 2.

By adjusting the polarization system, the three detections of the polarization parameter SPR imaging, intensity SPR imaging and the polarization contrast SPR imaging can be completed through program switching. Pure water is set as the extinction point. To compare different systems, intensity SPR imaging system needs to have the quarter-wave plate and analyzer removed and adjust the transmission axis of the polarizer to be parallel to the incident plane. In the polarization contrast SPR imaging, relative to the plane of incidence the polarizer sets to 60°. The angle of the quarter-wave plate is 0.9°, and the analyzer is set to 108° [38]. In the polarization parameter SPR imaging, the polarizer was modulated every 10° in a total cycle (180°). The camera used in the system is the acA2440-35um from the Basler Ace series. The acquisition result is an 8-bit image. The image is grayscale with pixel values ranging from 0 to 255.

Optics EXPRESS

4. Experiments result and discussion

We first use different concentrations of NaCl salute to verify the sensitivity of this system. For the best detection effect, only the middle 6 detection slots are used for the detection of six samples. Six detection tanks were sequentially injected with NaCl solution samples with six concentration gradients of 0%, 2.5%, 5%, 10%, 15% and 20%, the injection volume of each concentration of NaCl solution was the same is about 80 μL. The picture obtained after the inversion of the data obtained by the system is shown in Fig. 8. Figures 8(a) and 8(b) show the outcomes of the intensity SPR imaging system and polarization contrast SPR imaging system. In addition, Figs. 8(c) and 8(d) illustrate the results of the two parameters within the polarization parameter system. The values of the two parameters φ and $\sin\delta$ in the experiment represent the gray value of the φ map and $\sin\delta$ map obtained through calculation and inversion.

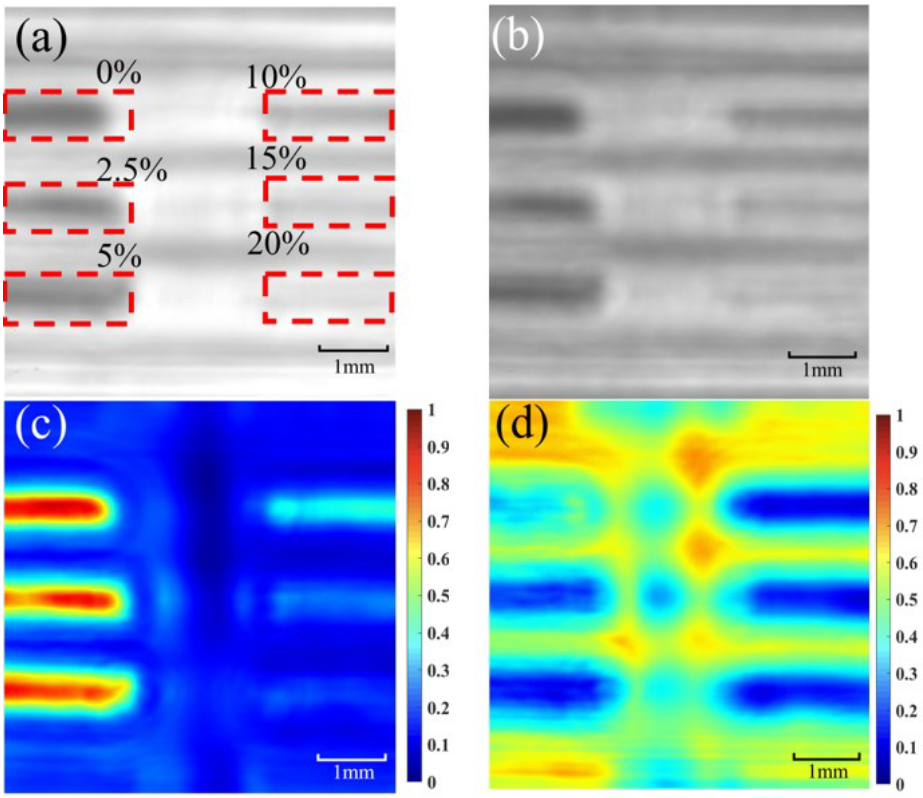

Fig. 8. Results of (a) intensity SPR imaging, (b) polarization contrast SPR imaging, (c) polarization parameters SPR imaging (φ), (d) polarization parameters SPR imaging (sinδ).

After scanning, the 19 original data images that were collected by the polarization parameter SPR imaging system in one cycle are calculated inversely, normalized and mapped back to the image. From this, φ and $\sin\delta$ can be obtained (see Fig. (9)).

From the grey value curve, the maximum value of the φ appears at the RI of pure water (1.3331) and gradually decreases when the reflective index increases from 1.3331 to 1.365. Within the reflective index range of 1.3331 to 1.3701, $\sin\delta$ curve trend is basically consistent with the changing trend of the theoretical curve, but there is a certain deviation for the rising section compared with the theoretical curve, and the rising range is small. This may be caused by

Optics EXPRESS

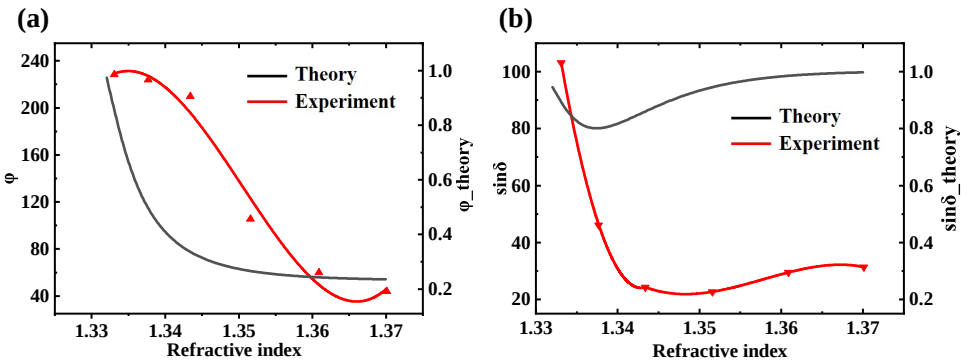

Fig. 9. The polarization parameter SPR imaging results. (a) Theory results and experiment results of φ. (b) Theory results and experiment results of sinδ.

the broadband of the light source. Because of the deviation of non-monochromatic light source, light source linewidth, film thickness, incident angle and polarization angle, systematic errors are inevitable. The calculation of the theoretical model is sensitive to the above parameters. This is the reason why we can see a huge difference between the theory and the raw data.

Figure 10 shows the sensitivity comparison of four different types of SPR imaging. We use the area-to-length ratio to determine the average sensitivity. In our research, we use the slope of the φ and sinδ curve as a measure of our system's sensitivity. When n is within the range of 1.34 to 1.36, the sensitivity trend and the position of the peak are consistent with the previous theoretical model calculations. Polarization parameter SPR imaging and intensity SPR imaging has a higher sensitivity than other SPR imaging method as confirmed by theoretical predictions. Within the reflective index range of 1.3331 to 1.34 of NaCl solution, the maximum sinδ sensitivity can reach 13000 RIU^{-1}, and the average sinδ sensitivity can reach 9500 RIU^{-1}. Within the range of 1.34 to 1.36, the maximum φ sensitivity can reach 9402 RIU^{-1}, and the φ average sensitivity can reach almost 8000 RIU^{-1}. Within this range, the polarization parameter SPR imaging φ sensitivity is about 5 times the normal polarization contrast SPR imaging and about 2.5 times the intensity SPR imaging. Within the range of 1.3331 to 1.34, the change of the sinδ is extremely significant. Compared with the polarization parameter SPR imaging (φ), polarization contrast SPR imaging and intensity SPR imaging, sinδ imaging has extremely high sensitivity, and φ imaging greatly complements the highly sensitive detection range of the polarization parameter SPR sinδ. Thus, high sensitivity and long detection range of the polarization parameter SPR imaging can be realized.

In addition, for the resolution and detection limit of this detection system, the baseline noise of the system is shown in Table. 2. Baseline noise is calculated by the pixel variance values of sinδ and φ maps within the central region of the air sample on the Microflow chip. Although the baseline noise of φ and sinδ of the polarization parameter SPR imaging are approximately 2.5 times and 3.5 times that of the baseline noise of the polarization contrast SPR imaging, its sensitivity is at least 5 times higher than the polarization contrast SPR imaging. Therefore, the resolution and detection limit of polarization parameter SPR imaging must be smaller than intensity SPR imaging and polarization contrast SPR imaging and has higher detection accuracy.

Finally, we use a polarization parameter SPR imaging system (three channels) to distinguish the H1N1 virus. In the virus experiment, we used H1N1 virus purchased from Guangzhou Ruida Biotechnology Co. Ltd. with a concentration of 1 mg/mL, which has been inactivated and has no pathogenicity. It was diluted to 1000 ng/mL with PBS buffer. Differing from the NaCl experiment, the virus sample adopts a physical evaporation method to immobilize the virus on the surface of the sensor chip, and the results are compared with air and PBS. Because our sensor

Optics EXPRESS

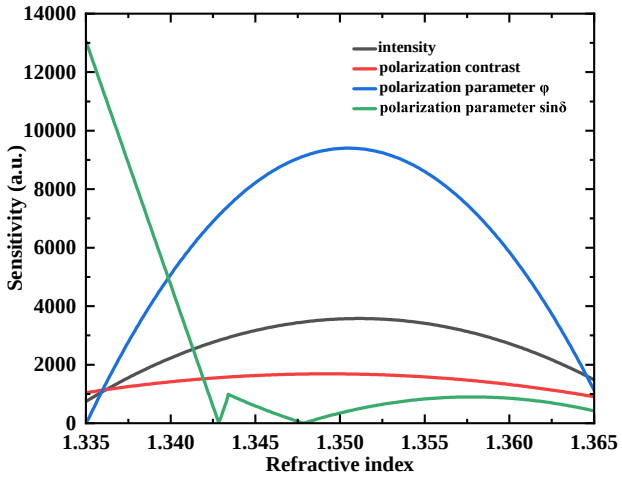

Fig. 10. Sensitivity comparison of four different types of SPR imaging.

Table 2. Three methods' baseline noise

Methods	Baseline noise(σ)
Intensity SPR imaging	**5.39**
Polarization contrast SPR imaging	**2.844**
Polarization parameter SPR imaging φ	**7.253**
Polarization parameter SPR imaging sinδ	**9.671**

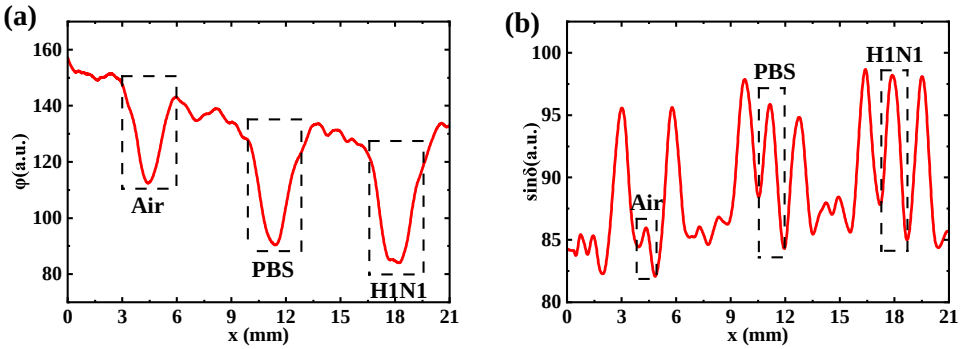

Fig. 11. The (a) φ and (b) sinδ H1N1 result curve of the change of the distance from the left end of the Microflow-Cell chip.

chip has not been biochemical modified, the virus can't be detected in solution, and the refractive index of the detection crystal formed by evaporation experiment can only be used for preliminary qualitative experiment, to illustrate the broad application prospects of the sensor in this paper.

The RI of virus was as high as 1.47 [39], the refractive of PBS with H1N1 is higher than the pure PBS, so the φ results of air, PBS, and H1N1 virus solution showed a decreasing trend in polarization parameter SPR imaging and the sinδ showed an increasing trend. The difference between the sinδ and φ is that the pixel of sinδ will appear two edge peaks around the bio-sample peaks. This may be helpful for locating bio-sample. In addition, although there is no effective functionalization method, the PBS curve part and the H1N1 curve part of the φ parameter and

Optics EXPRESS

sinδ parameter in Fig. 11. Axis x represents the location of the biological sample's distance from the Microflow-Cell chip left end.

5. Conclusion and outlook

In conclusion, in this paper polarization parameter SPR imaging is proposed, establishing theoretical modelling of polarization parameter SPR imaging, and showing the theoretical feasibility of polarization parameter SPR imaging as a RI sensor through model simulation. Based on the MATLAB multilayer film reflection model and the FDTD model, a detection system was simulated and a detection system was built. In the detection of NaCl solution, the polarization parameter SPR imaging showed better detection performance than other types of SPR imaging. In addition, the application of the polarization parameter SPR imaging in the field of virus detection is explored. Of course, there are further issues to be resolved, such as optimizing loading biological samples, more flexible polarizer adjustment methods and sensor functionalization. Additional research is required to develop a commercialized polarization SPR imaging sensor.

Funding. Natural Science Foundation of Jiangsu Province (BK20210326); Ministry of Education Collaborative Project (B17023); National Natural Science Foundation of China (62105155); Beijing Municipal Natural Science Foundation (Z190018); National Major Scientific Instruments and Equipment Development Project (61827814).

Acknowledgments. This work was supported by the National Major Scientific Instruments and Equipment Development Project (No. 61827814), Beijing Natural Science Foundation (No. Z190018), the National Natural Science Foundation of China (No. 62105155), the Ministry of Education collaborative project (B17023) and the Natural Science Foundation of Jiangsu Province (BK20210326). Special thanks to Houxiang Xu for his contribution to this research.

Disclosures. The authors declare no conflicts of interest.

Data availability. Data underlying the results presented in this paper are not publicly available at this time but may be obtained from the authors upon reasonable request.

References

1. S. A. Maier, *Plasmonics: Fundamentals and Applications* (Springer-Verlag, 2007) Chap. 1.
2. C. L. Nehl, H. Liao, and J. H. Hafner, "Optical properties of star-shaped gold nanoparticles," Nano Lett. **6**(4), 683–688 (2006).
3. A. V. Kabashin, P. Evans, S. Pastkovsky, *et al.*, "Plasmonic nanorod metamaterials for biosensing," Nat. Mater. **8**(11), 867–871 (2009).
4. C. Situ, M. H. Mooney, C. T. Elliott, *et al.*, "Advances in surface plasmon resonance biosensor technology towards high-throughput,food-safety analysis," TrAC, Trends Anal. Chem. **29**(11), 1305–1315 (2010).
5. Y. Li, Q. Liao, W. Hou, *et al.*, "Silver-Based Surface Plasmon Sensors: Fabrication and Applications," Int. J. Mol. Sci. **24**(4), 4142 (2023).
6. D. B. Axell-House, R. Lavingia, M. Rafferty, *et al.*, "The estimation of diagnostic accuracy of tests for COVID-19: A scoping review," J. Infect. **81**(5), 681–697 (2020).
7. J. S. Kahn, Y. Hu, and I. Willner, "Stimuli-responsive DNA-based hydrogels: from basic principles to applications," Acc. Chem. Res. **50**(4), 680–690 (2017).
8. R. Contreras-Cáceres, A. Sánchez-Iglesias, M. Karg, *et al.*, "Encapsulation and growth of gold nanoparticles in thermoresponsive microgels," Adv. Mater. **20**(9), 1666–1670 (2008).
9. W. Guo, C. H. Lu, X. J. Qi, *et al.*, "Switchable Bifunctional Stimuli-Triggered Poly-N-Isopropylacrylamide/DNA Hydrogels," Angew. Chem., Int. Ed. **53**(38), 10134–10138 (2014).
10. T. Xue, W. Liang, Y. Li, *et al.*, "Ultrasensitive detection of miRNA with an antimonene-based surface plasmon resonance sensor," Nat. Commun. **10**(1), 28 (2019).
11. L. Wu, H. S. Chu, W. S. Koh, *et al.*, "Highly sensitive graphene biosensors based on surface plasmon resonance," Opt. Express **18**(14), 14395–14400 (2010).
12. S. H. Choi, Y. L. Kim, and K. M. Byun, "Graphene-on-silver substrates for sensitive surface plasmon resonance imaging biosensors," Opt. Express **19**(2), 458–466 (2011).
13. M. Bocková, J. Slabý, T. Špringer, *et al.*, "Advances in surface plasmon resonance imaging and microscopy and their biological applications," Annu. Rev. Anal. Chem. **12**(1), 151–176 (2019).
14. E. Mauriz, A. Calle, J. J. Manclús, *et al.*, "Multi-analyte SPR immunoassays for environmental biosensing of pesticides," Anal. Bioanal. Chem. **387**(4), 1449–1458 (2007).
15. J. Divya, S. Selvendran, A. S. Raja, *et al.*, "Surface plasmon based plasmonic sensors: A review on their past, present and future," Biosens. Bioelectron.: X **11**, 100175 (2022).

Optics EXPRESS

16. J. Homola, "Surface plasmon resonance sensors for detection of chemical and biological species," Chem. Rev. **108**(2), 462–493 (2008).
17. P. O. Patil, G. R. Pandey, A. G. Patil, *et al.*, "Graphene-based nanocomposites for sensitivity enhancement of surface plasmon resonance sensor for biological and chemical sensing: A review," Biosens. Bioelectron. **139**, 111324 (2019).
18. K. Shrivas, R. Shankar, and K. Dewangan, "Gold nanoparticles as a localized surface plasmon resonance based chemical sensor for on-site colorimetric detection of arsenic in water samples," Sens. Actuators, B **220**, 1376–1383 (2015).
19. C. Zhan, X. J. Chen, Y. F. Huang, *et al.*, "Plasmon-mediated chemical reactions on nanostructures unveiled by surface-enhanced Raman spectroscopy," Acc. Chem. Res. **52**(10), 2784–2792 (2019).
20. B. Rothenhäusler and W. Knoll, "Surface–plasmon microscopy," Nature **332**(6165), 615–617 (1988).
21. Y. H. Huang, H. P. Ho, S. Y. Wu, *et al.*, "Detecting phase shifts in surface plasmon resonance: a review," Adv. Opt. Technol. **2012**, 1–12 (2012).
22. M. Piliarik, H. Vaisocherová, and J. Homola, "A new surface plasmon resonance sensor for high-throughput screening applications," Biosens. Bioelectron. **20**(10), 2104–2110 (2005).
23. Z. Huang, X. Wang, S. Zhan, *et al.*, "Contrast-enhancing polarization control method for surface plasmon imaging sensor," Opt. Eng. **51**(9), 094402-1 (2012).
24. W. Dong, K. Pang, Q. Luo, *et al.*, "Improved polarization contrast method for surface plasmon resonance imaging sensors by inert background gold film extinction," Opt. Commun. **346**, 1–9 (2015).
25. Y. Sun, H. Cai, and X. Wang, "Theoretical analysis of metamaterial-gold auxiliary grating sensing structure for surface plasmon resonance sensing application based on polarization control method," Opt. Commun. **405**, 343–349 (2017).
26. Y. Sun, H. Cai, X. Qiao, *et al.*, "High-performance polarization control modulated surface plasmon resonance sensor based on monolayer graphene/Au-NPs architecture for detection of DNA hybridization," Meas. Sci. Technol. **30**(12), 125701 (2019).
27. M. Piliarik and J. Homola, "Self-referencing SPR imaging for mostdemanding high-throughput screening applications," Sens. Actuators, B **134**(2), 353–355 (2008).
28. S. Patskovsky, R. Jacquemart, M. Meunier, *et al.*, "Phase-sensitive spatially-modulated surface plasmonresonance polarimetry for detection of biomolecular interactions," Sens. Actuators, B **133**(2), 628–631 (2008).
29. C. Y. Han and C. W. Luo, "An ellipsometric surface plasmon resonance system for quantitatively determining the normal of a sensor surface and multi-channel measurement," Opt. Commun. **294**, 8–12 (2013).
30. Y. Mikhyeyev and R. G. Sabat, "Polarization-contrast surface plasmon imaging," Opt. Express **28**(15), 21481–21488 (2020).
31. N. Liu, S. Wang, Q. Cheng, *et al.*, "Characteristics of refractive-index sensor in graphene-modified long-range surface exciton-polaritons," Plasmonics **16**(4), 1079–1088 (2021).
32. M. K. Singh, V. K. Verma, S. Pal, *et al.*, "Antimonene mediated long-range SPR imaging sensor with ultrahigh imaging sensitivity and figure of merit," Opt. Mater. **121**, 111484 (2021).
33. Y. Zeng, J. Zhou, W. Sang, *et al.*, "High-sensitive surface plasmon resonance imaging biosensor based on dual-wavelength differential method," Front. Chem. **9**, 801355 (2021).
34. N. Pal, J. B. Maurya, Y. K. Prajapati, *et al.*, "LiF-Ag-Si-TMDs based long-range SPR sensor in visible and NIR spectrum," Optik **274**, 170556 (2023).
35. S. Aghazadeh and H. Vahed, "Sensitivity enhancement of optical long-range SPR sensor based on new 2-d materials: Bp/mos2/graphene," PLASMONICS 1–15 (2023).
36. Y. Sun, H. Cai, and X. Wang, "Resonance plasmonic gold microwell arrays for high-performance surface plasmon resonance imaging based on polarization contrast modulation," J. Nanophoton. **13**(01), 1 (2018).
37. E. Kretschman and H. Raether, "Radiative decay of nonradiative surface plasmons excited by light," Z NATURFORSCH A **23**(12), 2135–2136 (1968).
38. S. Boshu, H. Zihao, and W. Xiaoping, "Intensity-modulated surface plasmon resonance array sensor based on polarization control," Guangxue Xuebao **31**(3), 0312003 (2011).
39. S. Chen and C. Lin, "High-performance bimetallic film surface plasmon resonance sensor based on film thickness optimization," Optik **127**(19), 7514–7519 (2016).